The following publication M. Liu, K. W. Chan, J. Hu, Q. Lin, J. Liu and W. Xu, "Design and Realization of a Coreless and Magnetless Electric Motor Using Magnetic Resonant Coupling Technology," in IEEE Transactions on Energy Conversion, vol. 34, no. 3, pp. 1200-1212, Sept. 2019 is available at https://doi.org/10.1109/TEC.2019.2894865.

Design and Realization of a Coreless and Magnetless Electric Motor using Magnetic Resonant Coupling Technology

Ming Liu, Ka Wing Chan, *Member, IEEE*,
Jiefeng Hu, *Senior Member, IEEE*, Qifang Lin, Junwei Liu, Wenzheng Xu

***Abstract*—Electric motors have a wide range of applications in a diverse range of industries. This paper presents a novel magnetic resonant coupling motor (MRCM) constructed without any iron or permanent-magnet core, i.e. a novel coreless and magnetless electric motor. Different from the conventional operation principle of existing electric motors, the application of the wireless power transfer (WPT) system using magnetic resonant coupling (MRC) technology is the key feature of the proposed MRCM. By adjusting the excitation frequency in accordance with the trajectory of resonant frequency splitting, a large electromagnetic force in different direction can be developed. Besides, the proposed MRCM has an inherent merit of unity power factor. This paper presents a new design concept, which could well be a promising start for a new generation of future electric motor.**

***Index Terms*—Coreless and magnetless, electric motor, frequency splitting, magnetic resonant coupling motor, wireless power transfer.**

I. Introduction

Electric motors, which lay the foundation of the modern industry, have a wide range of applications in automotive, machine tools, fans, refrigerators, pumps, industrial equipment and even toys. Various electric motors have been developed over the past century [1], such as induction motors (IMs) and permanent magnet synchronous motors (PMSMs). IMs take advantage of the electromagnetic induction to obtain the rotor current from the magnetic field of the stator winding. Iron cores are always utilized on stators or rotors to enhance the output torque as IMs without any iron cores would theoretically perform poorly due to the rather limited magnetic field density. For PMSMs, the usage of permanent magnets offers an independent magnetic field source. The electromagnetic torque can be developed through the interaction of magnetic field generated by permanent magnets and the stator winding. However, permanent magnets are expensive and suffer from the demagnetization at high temperature. Without permanent magnets and irons cores, PMSMs cannot work anymore. Using wireless power transfer (WPT), an attempt to configure an electric motor without any iron core or permanent magnet is proposed in this paper.

Due to the merits like space-saving, convenient and reliable, WPT method is a promising alternative to the conventional wire-based power delivery scheme [2-4]. Nikola Tesla initially proposed the concept of WPT, and employed the magnetic resonant coupling (MRC) technology in WPT in the early 20th century [5]. Since Kurs et al. presented a mid-range WPT system using the MRC technology in 2007 [6], the WPT system using MRC technology has drawn much attention in recent research. A great number of researchers have been studying and improving the WPT system using MRC technology for different applications, such as EV charger [7, 8] and biomedical implants [9, 10].

In a WPT system using MRC technology, frequency splitting phenomenon happens when the transmitter and receiver are in strong coupling condition. A great deal of research work has been conducted to investigate the frequency splitting phenomenon ranging from two-coil WPT system [11, 12], to three-coil WPT system [13], and further to four-coil WPT system [14, 15]. The frequency splitting phenomenon concerns the frequency characteristics of transfer power, while the maximum system efficiency is always at the natural resonant frequency. Most studies of frequency splitting phenomenon refer to the perspective of transferring power. Some researchers employ the frequency tracking methodology, where the excitation frequency is varying with different coupling coefficient, to maintain the optimal power transfer [16, 17]. Other researchers have proposed some frequency splitting suppression methods, like adjusting the load resistor [18] and using nonidentical resonant coils [19], to obtain uniform power on the receiver side. The main application of WPT system using MRC technology is to transfer power in stationary state. The specific application of WPT system using MRC technology in rotating state has been reported in [20]. Besides, a near field inductive communication scheme has been developed by manipulating the frequency splitting phenomenon [21]. With the manipulation of the frequency splitting phenomenon, a potential application of the WPT system using MRC technology in electric motor is demonstrated in this paper.

This paper presents a novel magnetic resonant coupling motor (MRCM) and without any iron or permanent-magnet core. The application of the WPT system using MRC technology is the key feature of the proposed MRCM. Different from paper [22] where a motor is powered by WPT system

The authors gratefully acknowledge the support of the Hong Kong Polytechnic University (RU3S, RUB1, 1-ZE7J and G-YBZ4), Hong Kong PhD Fellowship (RUYQ), and Innovation and Technology Fund (ITS/037/14).

M. Liu, K.W. Chan, J.F. Hu, Q.F. Lin, J.W. Liu, and W.Z. Xu are with the Department of Electrical Engineering, The Hong Kong Polytechnic University (e-mail: leo.m.liu@connect.polyu.hk, eekwchan@polyu.edu.hk, jerry.hu@polyu.edu.hk, qfang.lin@connect.polyu.hk, jun-wei.liu@connect.polyu.hk, wen-zheng.xu@connect.polyu.hk)

Corresponding author: K. W. Chan, e-mail: eekwchan@polyu.edu.hk.

using MRC technology, the proposed MRCM would develop the output torque by the WPT system using MRC technology, in which the frequency splitting phenomenon would not be suppressed, but be utilized. By manipulating the phase characteristics of frequency splitting phenomenon, large torque in different direction is achievable through the manipulation of excitation frequency. Presently, coil-to-coil WPT efficiencies of over 90% at multiple kW have been reported [23, 24], and would be an indication to the potential high efficiency of the proposed MRCM. Coupled with the small distance (a few millimeters) between stator and rotor power-transfer coils, the efficiency could be further enhanced. The proposed MRCM is a new generation of coreless and magnetless electric motor with the following merits:

1) Lighter in weight, no core loss and no flux saturation problem due to the coreless and magnetless design.
2) The proposed MRCM has an inherent characteristic of unity power factor irrespective of the load condition.
3) The magnitude and direction of the output torque can be manipulated easily through the control of the excitation frequency.
4) The rotor can extract power from the stator to power devices installed on the rotor side, irrespective of the motor being rotating or not.

This paper is organized as follows. In Section II, the resonant topology is first selected with the consideration of the phase characteristics. Then, the underlying operation principle of the proposed MRCM is presented from the perspective of an elementary pole pair in Section III. The magnitude and direction of the force in a pole pair, frequency splitting phenomenon, and the trajectory of resonant splitting frequency are discussed in this section. In addition, in Section IV, the design procedure is demonstrated, and the simulations results using MAXWELL, PSIM and ANSYS Maxwell are presented to validate the feasibility of the proposed MRCM. Finally, the paper is concluded in Section V.

II. Selection of Resonant Topology

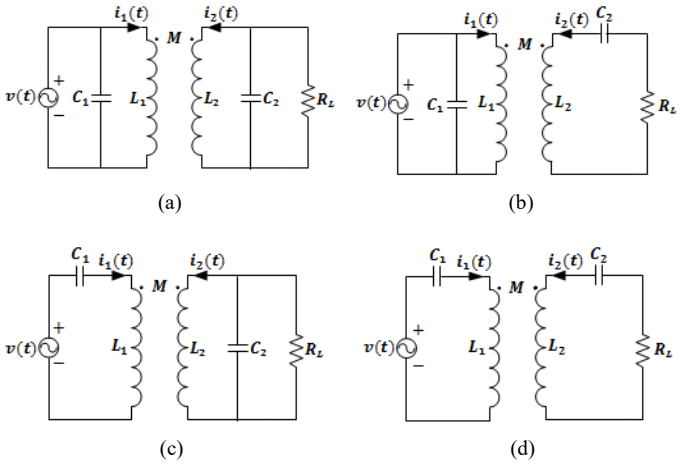

Fig. 1. Resonant topologies for two-resonant-circuit WPT system. (a) parallel-parallel (PP) resonant topology. (b) parallel-series (PS) resonant topology. (c) series-parallel (SP) resonant topology. (d) series-series (SS) resonant topology.

Considering two-resonant-circuit WPT system with one transmitter resonant circuit and one receiver resonant circuit, each resonant circuit could be either in series LC resonant topology or parallel LC resonant topology. Neglecting internal resistances, four different LC resonant topologies are depicted in Fig. 1.

To transfer power efficiently, transmitter resonant circuit and receiver resonant circuit are tuned to be resonant at a same natural frequency ω_0 (or f_0), which merely depends on the inductance L and capacitance C,

$$\omega_0 = \frac{1}{\sqrt{LC}} \tag{1}$$

$$f_0 = \frac{\omega_0}{2\pi} = \frac{1}{2\pi\sqrt{LC}} \tag{2}$$

Using a general expression, the equivalent equation for four resonant topologies can be written as:

$$Z\begin{bmatrix}\dot{I}_1\\ \dot{I}_2\end{bmatrix} = \begin{bmatrix}V\\ 0\end{bmatrix} \tag{3}$$

where $\dot{I}_1$ and $\dot{I}_2$ are the fundament current phasor of transmitter resonant circuit and receiver resonant circuit respectively. V is the RMS (Root Mean Square) value of the input sin-wave voltage. Z is the impedance matrix, which has four different forms (4)-(7) corresponding to four resonant topologies as are shown in Fig. 1. (a), (b), (c) and (d).

$$Z_{PP} = \begin{bmatrix}j\omega L_1 & j\omega M\\ j\omega M & j\omega L_2 + R_L\end{bmatrix} \tag{4}$$

$$Z_{PS} = \begin{bmatrix}j\omega L_1 & j\omega M\\ j\omega M & j\omega L_2 + \frac{1}{j\omega C_2} + R_L\end{bmatrix} \tag{5}$$

$$Z_{SP} = \begin{bmatrix}j\omega L_1 + \frac{1}{j\omega C_1} & j\omega M\\ j\omega M & j\omega L_2 + R_L\end{bmatrix} \tag{6}$$

$$Z_{SS} = \begin{bmatrix}j\omega L_1 + \frac{1}{j\omega C_1} & j\omega M\\ j\omega M & j\omega L_2 + \frac{1}{j\omega C_2} + R_L\end{bmatrix} \tag{7}$$

where R_L are the equivalent resistance of the load. L_1 and L_2 are the inductances of the transmitter resonant circuit and receiver resonant circuit respective. C_1 and C_2 are the capacitances of the transmitter resonant circuit and receiver resonant circuit respective. ω is the excitation frequency in rad/s. M is the mutual inductance which represents the interlink degree of the magnetic field between the transmitter resonant circuit and receiver resonant circuit.

A. Investigation of Phase Difference δ

The generalized equivalent circuits at the transmitter side and receiver side are depicted in Fig. 2.

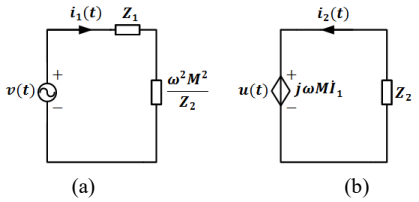

Fig. 2. Equivalent circuits. (a) at transmitter side. (b) at receiver side.

Using the equivalent circuit as is shown in Fig. 2(a), the fundamental current phasor can be derived as:

$$\dot{I}_1 = \frac{V}{Z_1 + \frac{\omega^2 M^2}{Z_2}} \tag{8}$$

The magnitude of $\dot{I}_1$ is not only determined by the transmitter

impedance Z_1, but the reflected impedance $\frac{\omega^2 M^2}{Z_2}$.

At the receiver side as is shown in Fig. 2(b), the fundamental voltage phasor $\dot{U}$ of the controlled voltage source is

$$\dot{U} = j\omega M \dot{I}_1 \tag{9}$$

Comparing the expressions of $\dot{U}$ and $\dot{I}_1$, there is a complex angle j which indicates that the phase difference between $\dot{U}$ and $\dot{I}_1$ is 90° ($\dot{U}$ is 90° ahead of $\dot{I}_1$). In other words, the phase difference between $\dot{U}$ and $\dot{I}_1$ is independent of the resonant topology of transmitter resonant circuit. At the transmitter side, both series and parallel resonant topologies always result in a 90° phase difference between $\dot{U}$ and $\dot{I}_1$.

The fundamental phasor current $\dot{I}_2$ at the receiver side is derived as

$$\dot{I}_2 = \frac{\dot{U}}{Z_2} \tag{10}$$

The phase angle of $\dot{I}_2$ is determined by Z_2. Assuming no resistance component in Z_2, an inductive Z_2 indicates that $\dot{I}_2$ is 90° ahead of $\dot{U}$, while a capacitive Z_2 indicates that $\dot{I}_2$ lags 90° behind of $\dot{U}$. As the phase difference between $\dot{U}$ and $\dot{I}_1$ is always 90°, the former case results in that the phase difference δ between $\dot{I}_1$ and $\dot{I}_2$ is 180°, while the latter case results in that the phase difference δ between $\dot{I}_1$ and $\dot{I}_2$ is 0°. To sum up, the inductive or capacitive characteristic of Z_2 determines the phase difference δ between $\dot{I}_1$ and $\dot{I}_2$, but the transmitter side has no effect on the phase difference δ between $\dot{I}_1$ and $\dot{I}_2$.

B. Selection of Resonant Topology

The proposed MRCM would be composed of many paired transmitter and receiver resonant circuits, and the force is generated by the paired resonant circuits. Based on Ampere's Law, if the direction of the current flowing in two current carrying wires is the same, two wires attracts each other; on the contrary, if the direction of the current flowing in two current carrying wires is opposite, two wires repels each other. Hence, when transmitter and receiver resonant circuits have the same corresponding terminals to define the current direction, an attraction force would be generated when phase difference δ between $\dot{I}_1$ and $\dot{I}_2$ is 0°, while an repulsion force would be generated when phase difference δ between $\dot{I}_1$ and $\dot{I}_2$ is 180°. It is preferable to select a suitable resonant topology to develop both attraction force and repulsion force to enhance the capability of force generation.

Fig. 3 shows the simulation results of the phase difference δ between $\dot{I}_1$ and $\dot{I}_2$ for different excitation frequency for four resonant topologies. In Fig. 3(a), PP and SP resonant topologies present a consistent 0° phase difference δ for different excitation frequency, which means that parallel resonant topology of the receiver resonant circuit always presents a Z_2 in capacitive characteristic irrespective of the different excitation frequency. For P-S and S-S resonant topologies, Fig. 3(b) demonstrates that both 0° and 180° phase difference δ between $\dot{I}_1$ and $\dot{I}_2$ are achievable. For the receiver resonant circuit in series resonant topology, the impedance Z_{2S} is

$$Z_{2S} = j\omega L_2 + \frac{1}{j\omega C_2} \tag{11}$$

As both inductive Z_{2S} (when $f > f_0$) and capacitive Z_{2S} (when $f < f_0$) are achievable, receiver resonant circuit in series resonant topology is selected to generate both repulsion force and attraction force.

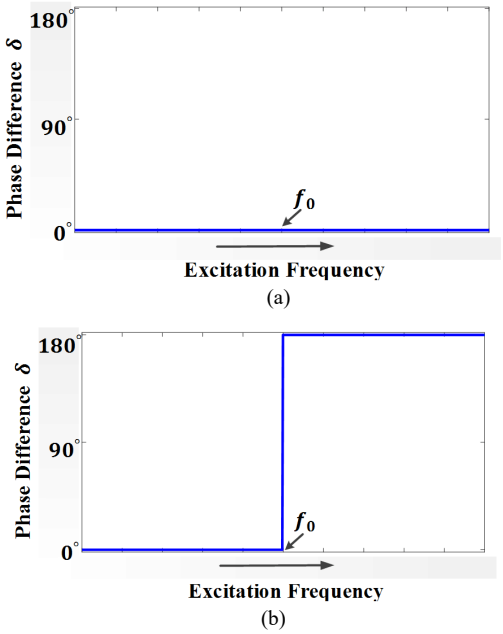

Fig. 3. Phase difference δ between $\dot{I}_1$ and $\dot{I}_2$ for different excitation frequency. (a) P-P and S-P resonant topologies. (b) P-S and S-S resonant topologies.

Regarding to the topology in transmitter side, the series resonant topology presents the minimum impedance value when the circuit is in resonant state, and a large current would be developed. Besides, the series resonant method has better response to the fluctuations of the coupling coefficient [25]. A series resonant topology is therefore employed to configure the transmitter resonant circuit in order to maximize the current magnitude. Consequently, both transmitter resonant circuit and receiver resonant circuit should be configured as series resonant topology to achieve maximum attraction or repulsion force.

III. Pole Pair Analysis

The basic operation principle of this novel MRCM is illustrated in this section. A single pole pair as shown in Fig. 4 consists of two resonant circuits with series resonant topology. The material of stator and rotor cores is reinforce plastic.

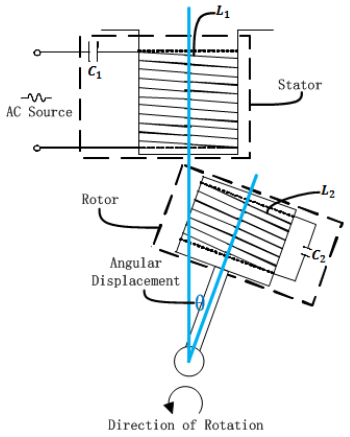

Fig. 4. A pole pair in the proposed MRCM.

The transmitter resonant circuit is referred as stator resonant circuit which is operable to generate an alternating magnetic field in response to a supplied sine-wave voltage, while the receiver resonant circuit is served as the rotor resonant circuit which is an independent closed circuit. The stator resonant circuit and the rotor resonant circuit are configured to have the same natural frequency ω_0 (or f_0). All stator or rotor windings should be configured with the same geometry and symmetrical to avoid the adverse impact of end winding. Then, the equivalent circuit of a pole pair is shown in Fig. 5.

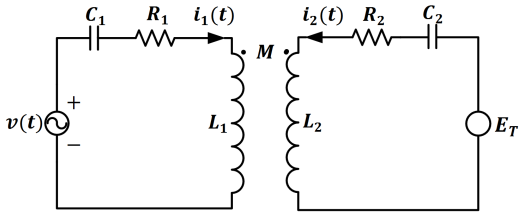

Fig. 5. Equivalent circuit of a pole pair

Using the circuit theory, the relationship between the fundamental current phasor I_1 of transmitter resonant circuit, the fundamental current phasor I_2 of receiver resonant circuit, and the input RMS voltage V can be obtained as follows:

$$\begin{bmatrix} j\omega L_1 + \frac{1}{j\omega C_1} + R_1 & j\omega M \\ j\omega M & j\omega L_2 + \frac{1}{j\omega C_2} + R_2 \end{bmatrix} \begin{bmatrix} \dot{I}_1 \\ \dot{I}_2 \end{bmatrix} = \begin{bmatrix} V \\ 0 \end{bmatrix} \quad (12)$$

The RMS current I_1 and I_2 in stator and rotor resonant circuits can be derived as

$$I_1 = \frac{V\sqrt{\left(\omega L_2 - \frac{1}{\omega C_2}\right)^2 + {R_2}^2}}{\sqrt{A^2+B^2}} \quad (13)$$

$$I_2 = \frac{Vk\omega\sqrt{L_1 L_2}}{\sqrt{A^2+B^2}} \quad (14)$$

where

$$A = R_1\left(\omega L_2 - \frac{1}{\omega C_2}\right) + R_2\left(\omega L_1 - \frac{1}{\omega C_1}\right)$$

$$B = R_1 R_2 - \left(\omega L_1 - \frac{1}{\omega C_1}\right)\left(\omega L_2 - \frac{1}{\omega C_2}\right) + k^2\omega^2 L_1 L_2$$

R_1 and R_2 are the internal resistance of stator and rotor resonant circuit respectively. E_T represents the output. k is the coupling coefficient which indicates the coupling degree between the stator resonant circuit. The relationship between coupling coefficient k and mutual inductance M is

$$k = \frac{M}{\sqrt{L_1 L_2}} \quad (15)$$

A. Natural Frequency

For any WPT system, it is necessary to the select a suitable natural frequency f_0. The employment of higher natural frequency f_0 has merits including more compact, higher quality factor and longer transmission distance, but demands more expensive drive and control system.

As stator and rotor resonant circuits are special oscillation circuits, a process of starting oscillation is essential for each effective pole pair. As is indicated in Fig. 6, certain number of periods is needed to achieve a complete oscillation for resonant circuits in an effective pole pair. Since period is inversely proportional to the natural frequency f_0, the magnitude of natural frequency therefore determines the duration of starting oscillation process, and affects the performance of the proposed MRCM.

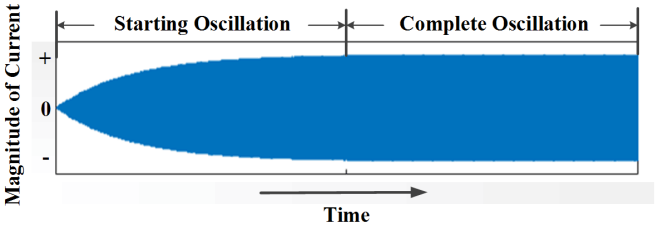

Fig. 6. Starting oscillation and complete oscillation in stator or rotor resonant circuit.

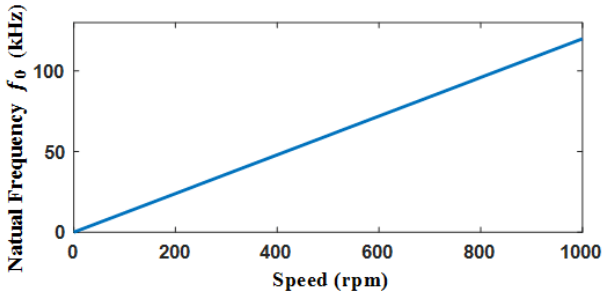

Fig. 7. Natural frequency f_0 for achieving complete oscillation within 5° rotation against speed

For a rotor to rotate in a certain speed, a suitable natural frequency has to be selected to guarantee that stator and rotor resonant circuits can achieve the complete oscillation in a short time to generate maximum output electromagnetic force. For example, if the complete oscillation can be fulfilled in one hundred periods within 5° rotation, the relation between speed and natural frequency is depicted in Fig. 7, which could serve as a guideline for selecting the natural frequency f_0.

B. Force Magnitude and Direction

From the aforementioned analysis of topology selection, the phase difference δ between $\dot{I}_1$ and $\dot{I}_2$ determines the direction of the force developed in a pole pair. Moreover, the phase difference δ between $\dot{I}_1$ and $\dot{I}_2$ can affect the magnitude of the force developed in a pole pair. With the consideration of internal resistances, the expression of the phase difference δ between $\dot{I}_1$ and $\dot{I}_2$ is derived as

$$\delta = arctan\frac{R_2}{\frac{1}{\omega C_2} - \omega L_2} \quad (16)$$

For a pole pair, when $R_2 = 0$ or $R_2 > 0$, the locus of the phase difference δ between $\dot{I}_1$ and $\dot{I}_2$ for difference excitation frequency is plotted in Fig. 8.

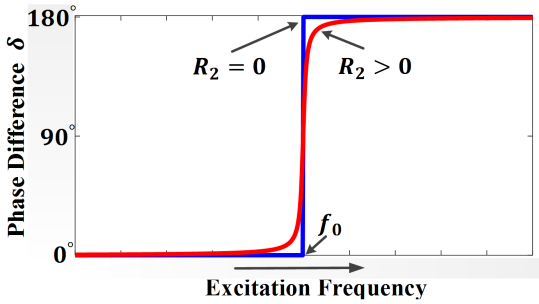

Fig. 8. Phase difference δ between $\dot{I}_1$ and $\dot{I}_2$ for difference excitation frequency for a pole pair when $R_2 = 0$ or $R_2 > 0$.

Due to the existence of R_2, the phase difference δ between $\dot{I}_1$ and $\dot{I}_2$ is no longer exactly 0° (when $f < f_0$) or 180° (when $f > f_0$), which would deteriorate the force developed in a pole pair. Besides, large values of R_2 in the rotor resonant circuit would also worsen the performance. Therefore, a smaller resistance value in rotor resonant circuit is preferable. Here, an attenuation coefficient γ is introduced to represent the magnitude and direction of the force developed in a pole pair.

$$\gamma = \frac{\int_0^{2\pi} sin(t)sin(t-\delta)}{\int_0^{2\pi} sin^2(t)} = cos\delta \tag{17}$$

When the excitation frequency f is smaller than f_0, the phase difference δ between $\dot{I}_1$ and $\dot{I}_2$ is in the range of $0^\circ \leq \delta < 90^\circ$. The attenuation coefficient γ is thus in the range of $0 < \gamma \leq 1$. Positive value of γ means an attraction force can be generated, and the maximal attraction force is achievable when $\gamma = 1$. Besides, when the excitation frequency f is greater than f_0, the phase difference δ between $\dot{I}_1$ and $\dot{I}_2$ is in the range of $90^\circ < \delta \leq 180^\circ$. The attenuation coefficient γ is therefore in the range of $-1 \leq \gamma < 0$. Negative value of γ means a repulsion force can be generated, and the maximal repulsion force is achievable when $\gamma = -1$. Moreover, no force would be generated in a pole pair when γ is equal to 0, and excitation frequency f is equal to f_0.

While the sign of attenuation coefficient γ determines the direction of the force in a pole pair, its magnitude can affect but not determine the magnitude of the force in a pole pair. To achieve a maximum force magnitude in a pole pair, the excitation frequency has to follow the frequency splitting trajectory for different angular displacement θ.

C. *Frequency Splitting Phenomenon*

The angular displacement θ shown in Fig. 4 indicates the position of the rotor resonant circuit relative to the stator resonant circuit. For a specific value of the angular displacement θ, there is a corresponding value of the coupling coefficient k.

In the strong coupling condition, where the coupling coefficient k is greater than the critical coupling coefficient k_c, the optimal excitation frequency to achieve the maximum values of I_1 and I_2 splits into two specific frequency sets. It is the frequency splitting phenomenon as shown in Fig. 9.

The critical coupling coefficient k_c can be derived as follows. By letting $\omega = \omega_0$ in (17), I_2 is

$$I_2 = \frac{V\omega_0 k\sqrt{L_1L_2}}{R_1R_2+k^2\omega_0{}^2L_1L_2} \tag{18}$$

The first derivative of I_2 to k is

$$\frac{dI_2}{dk} = \frac{V\omega_0\sqrt{L_1L_2}(R_1R_2-k^2\omega_0{}^2L_1L_2)}{(R_1R_2+k^2\omega_0{}^2L_1L_2)^2} \tag{19}$$

Then, solving k for $\frac{dI_2}{dk} = 0$. The value of k_c is analytically derived as

$$k_c = \sqrt{\frac{R_1R_2}{\omega_0{}^2L_1L_2}} = \frac{1}{\sqrt{Q_1Q_2}} \tag{20}$$

where Q_1 and Q_1 are the quality factor for stator resonant circuit and rotor resonant circuit respectively. The stator and rotor resonant circuits in a pole pair should always be configured to have a coupling coefficient k which is always greater than critical coupling coefficient k_c.

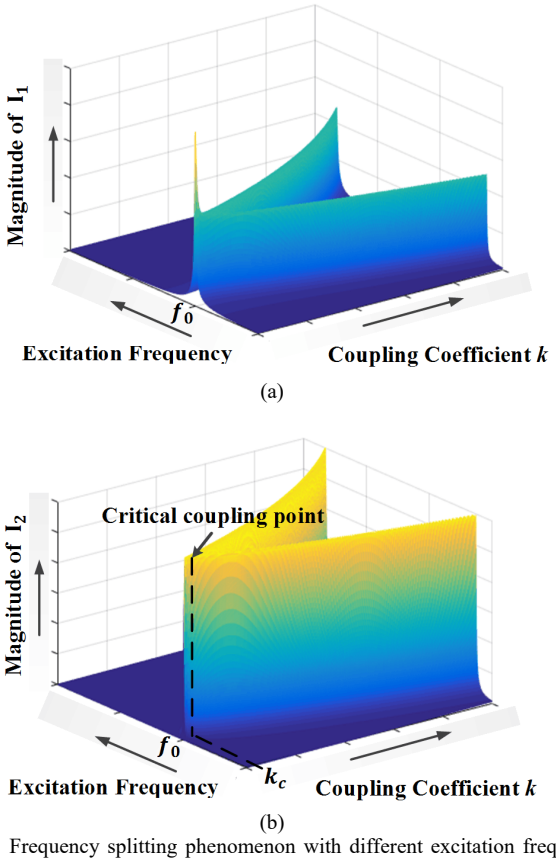

Fig. 9. Frequency splitting phenomenon with different excitation frequency and coupling coefficient for (a) I_1 and (b) I_2.

D. *Lower/Higher Resonant Splitting Frequency*

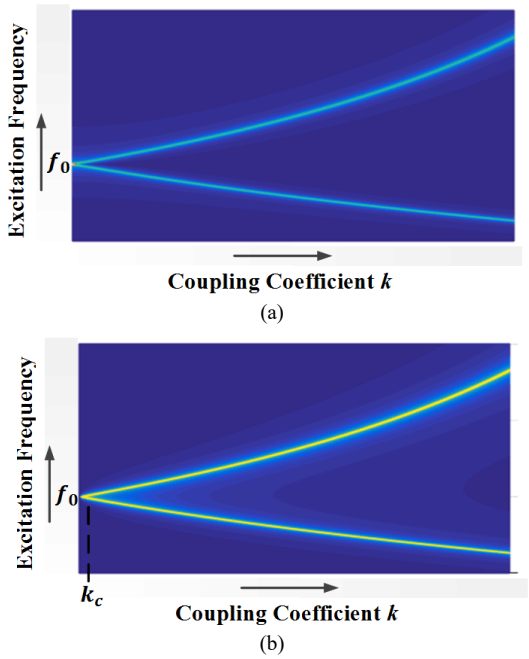

Fig. 10. Trajectory of lower resonant splitting frequency f_L and higher resonant splitting frequency f_H. (a) in the view of I_1. (b) in the view of I_2.

For the aforementioned two frequency sets to achieve the maximum values of I_1 and I_2, one set of which is lower than the natural frequency f_0, named as the lower resonant splitting frequency f_L, while the other higher than the natural frequency f_0 is named as the higher resonant splitting frequency f_H. The

trajectory of lower resonant splitting frequency f_L and higher resonant splitting frequency f_H are shown in Fig. 10, where I_1 and I_2 have the same trajectory of lower resonant splitting f_L and higher resonant splitting frequency f_H.

The lower resonant splitting frequency f_L and higher resonant splitting frequency f_H can be derived as follows. With the assumption of no resistances, the undamped natural response is

$$\begin{bmatrix} 1-\frac{{\omega_0}^2}{\omega^2} & k\sqrt{\frac{L_2}{L_1}} \\ k\sqrt{\frac{L_1}{L_2}} & 1-\frac{{\omega_0}^2}{\omega^2} \end{bmatrix}\begin{bmatrix} I_1 \\ I_2 \end{bmatrix}=\begin{bmatrix} 0 \\ 0 \end{bmatrix} \tag{21}$$

The assumption of neglecting the internal resistances is reasonable since internal resistances are usually much smaller than the resonant impedance ωL and $\frac{1}{\omega C}$. (21) can be rearranged as

$$\frac{{\omega_0}^2}{\omega^2}\begin{bmatrix} I_1 \\ I_2 \end{bmatrix}=\begin{bmatrix} 1 & k\sqrt{\frac{L_2}{L_1}} \\ k\sqrt{\frac{L_1}{L_2}} & 1 \end{bmatrix}\begin{bmatrix} I_1 \\ I_2 \end{bmatrix} \tag{22}$$

where $\frac{{\omega_0}^2}{\omega^2}$ is the eigenvalue of the matrix A, which is written as

$$A=\begin{bmatrix} 1 & k\sqrt{\frac{L_2}{L_1}} \\ k\sqrt{\frac{L_1}{L_2}} & 1 \end{bmatrix} \tag{23}$$

The eigenvalue of matrix A can be calculated as

$$\frac{{\omega_0}^2}{\omega^2}=1+k, 1-k \tag{24}$$

The expressions of lower resonant splitting frequency f_L and higher resonant splitting frequency f_H are therefore derived as

$$f_L=\frac{\omega_0}{2\pi\sqrt{1+k}}, f_H=\frac{\omega_0}{2\pi\sqrt{1-k}} \tag{25}$$

Equation (25) of the lower resonant splitting frequency f_L and higher resonant splitting frequency f_H are the function of coupling coefficient k. Since coupling coefficient k is directly related to the angular displacement θ, the values of lower resonant splitting frequency f_L and higher resonant splitting frequency f_H correspond to the angular displacement θ. As the force generated in a pole pair is directly proportional to the magnitude of I_1 and I_2, the highest magnitude of I_1 and I_2 is preferred. To achieve maximum magnitude of I_1 and I_2, and thus to generate the possible maximum force in a pole pair, the excitation frequency f must follow the trajectory of lower resonant splitting frequency f_L and higher resonant splitting frequency f_H.

E. Power Factor

The power factor (PF) is defined as the ratio of the real power to the apparent power. Unity PF is preferable for all electric-motor loads since higher PF indicates lower cost and higher efficiency. Most conventional electric motors, such as IMs and PMSMs, has relatively poor PFs (< 0.9), though capacitors are installed to compensate the inductance of copper winding.

In an electric motor, PF can be represented by the phase difference between the input voltage and current. Based on (12), the phase difference φ between V and $\dot{I}_1$ can be derived as

$$\varphi = arctan\frac{(\omega L_1-\frac{1}{\omega C_1})-\frac{\omega^2M^2(\omega L_2-\frac{1}{\omega C_2})}{{R_2}^2+(\omega L_2-\frac{1}{\omega C_2})^2}}{R_1+\frac{\omega^2M^2R_2}{{R_2}^2+(\omega L_2-\frac{1}{\omega C_2})^2}} \tag{26}$$

and PF can then be calculated as

$$\text{PF}=\cos\varphi \tag{27}$$

When applying lower resonant splitting frequency f_L and higher resonant splitting frequency f_H, the variation of PF can be depicted as is shown in Fig. 11. Smaller value of R_2 and smaller absolute value of angular displacement θ corresponds to higher PF for the proposed MRCM. Since R_2 is usually small, the power factor of the proposed MRCM is close to unity.

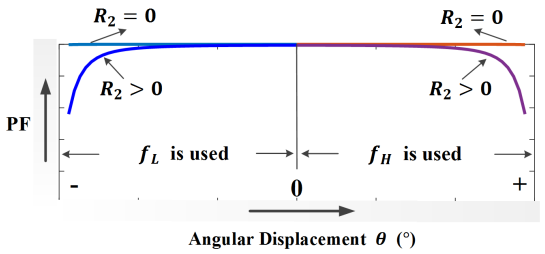

Fig. 11. Variation of PF corresponding to different angular displacement θ and different R_2.

F. Operation Principle

From the perspective of a pole pair, the underlying operation principle is illustrated as follows. As shown in Fig. 12(a), when the rotor resonant circuit is approaching the stator resonant circuit, for different angular displacement θ, the stator resonant circuit would be powered with the trajectory of the low resonant splitting frequency f_L to generate the possible maximum force. At such a circumstance, as the phase difference δ between $\dot{I}_1$ and $\dot{I}_2$ is 0°, the stator and rotor poles would have the same polarity. An attraction force can be therefore developed between the stator resonant circuit and the adjacent rotor resonant circuit.

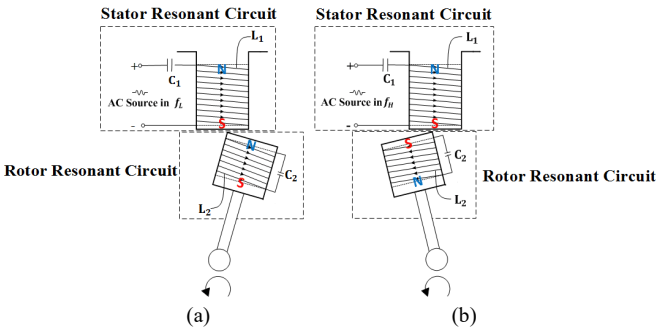

Fig. 12. Polarity demonstration for a pole pair with excitation frequency in (a) lower resonant frequency f_L (b) higher resonant frequency f_H.

Furthermore, as shown in Fig. 12(b), when the rotor resonant circuit is leaving the stator resonant circuit, for different angular displacement θ, the stator resonant circuit would be powered with the trajectory of the high resonant splitting frequency f_H to generate the possible maximum force. In this case, as the phase difference δ between $\dot{I}_1$ and $\dot{I}_2$ is 180°, the stator and rotor poles would have the opposite polarity. A repulsion force can thus be developed between them. With the coordination of those attraction and repulsion forces, the rotor

could be driven to rotate and operates as an electric motor. Besides, different arrangement of pole number and pole ratio could be developed based on such a pole pair.

IV. Design Guideline and Validation

The pole pair is the fundamental element of a complete MRCM, and different pole-ratio arrangement could be further optimized based on the pole pair. Therefore, simulation results shown in this section are from the perspective of a single pole pair. The basic design procedures are demonstrated in Fig. 13.

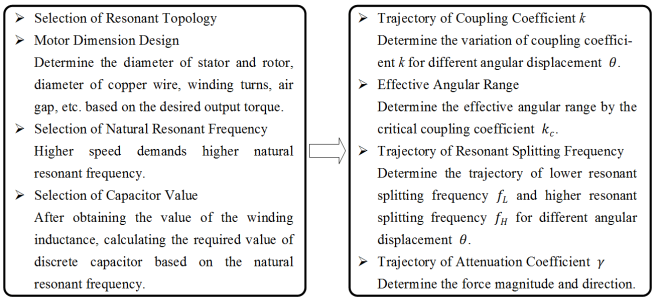

Fig. 13. Basic design procedures for the proposed MRCM

The proposed MRCM has been comprehensively validated using computer simulations in MATLAB, PSIM and ANSYS Maxwell. As shown in Fig. 14, a 2D pole pair model is firstly developed in ANSYS Maxwell. The constructional dimension and technical parameters are listed in Table I with practical consideration.

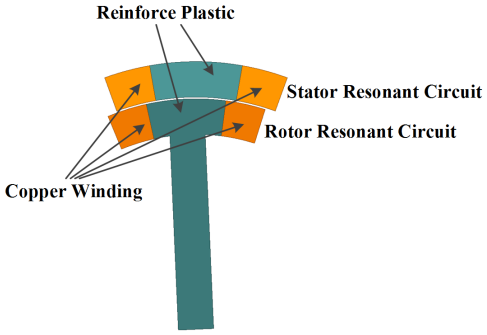

Fig. 14. A 2D pole pair model in ANSYS Maxwell

A. k, f_L, f_H and γ

The self-inductance and mutual inductance of stator and rotor windings at different angular displacement θ is simulated using the 2D model of Fig. 14. The coupling coefficient k is then calculated by (15), and the fitting curve of coupling coefficient k at different angular displacement θ is depicted in Fig. 15.

Substituting parameters in Table I into (20), k_c is calculated to be 0.0035. The corresponding angular displacement θ for k_c is around $\pm 14°$, which is the effective angular range for a pole pair.

Combining the simulation results of coupling coefficient k in Fig. 15 and the analytical expression in (25), the trajectory of lower resonant splitting frequency f_L and higher resonant splitting frequency f_H corresponding to different angular displacement θ can be calculated and depicted in Fig. 16.

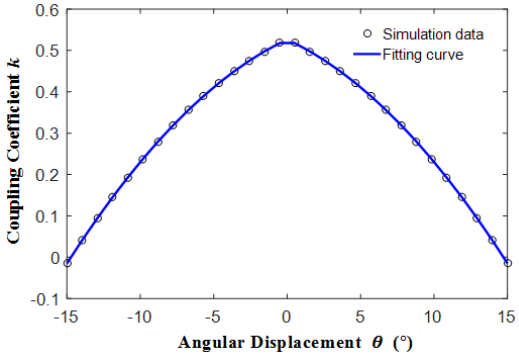

Fig. 15. Simulation result from ANSYS Maxwell: coupling coefficient k corresponding to different angular displacement θ

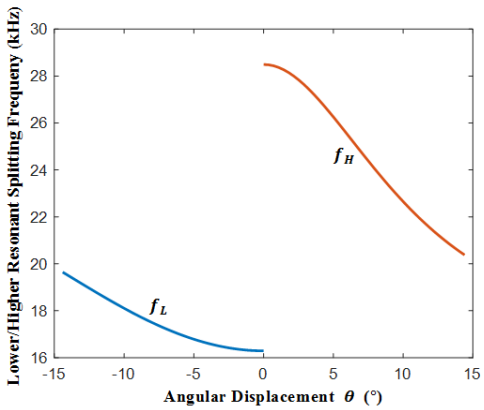

Fig. 16. Simulation result from MATLAB: trajectory of lower resonant splitting frequency f_L and higher resonant splitting frequency f_H corresponding to different angular displacement θ

When the excitation frequency follows the trajectory of lower resonant splitting frequency f_L and higher resonant splitting frequency f_H as shown in Fig. 16, the magnitude of attenuation coefficient γ corresponding to different angular displacement θ can be obtained. As is shown in Fig. 17, the attenuation coefficient γ is approximately -1 when the lower resonant splitting frequency f_L is used, while the attenuation coefficient γ is approximately 1 when the higher resonant splitting frequency f_H is used. Fig. 17 indicates that, due to the small resistance value in the rotor resonant circuit, the possible maximum attraction and repulsion forces are achievable by using the lower resonant splitting frequency f_L and higher resonant splitting frequency f_H as the excitation frequency.

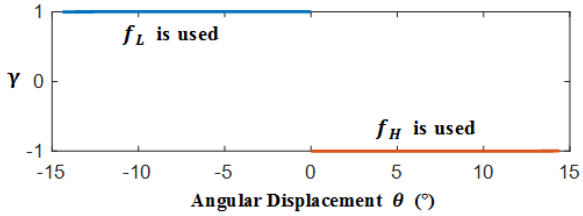

Fig. 17. Simulation result from MATLAB: the magnitude of attenuation coefficient γ corresponding to different angular displacement θ when f_L or f_H is used as the excitation frequency.

With the R_2 in Table I, the magnitude of PF corresponding to different angular displacement θ can be obtained from the simulation as is shown in Fig. 18. A unity power factor can be maintained at all angular displacement θ for the proposed MRCM.

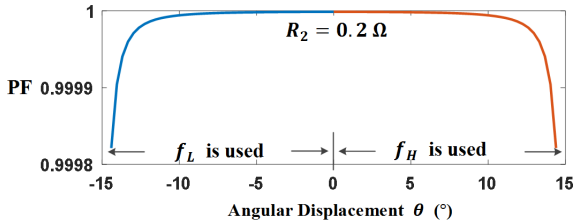

Fig. 18. Simulation result from MATLAB: the magnitude of PF corresponding to different angular displacement θ with $R_2 = 0.2\ \Omega$.

B. RMS Currents and Average Torque

Using the data obtained in Fig. 15-17, the magnitudes of RMS current I_1 and I_2 corresponding to different angular displacement θ are then simulated in PSIM. As is shown in Fig. 19, blue curve is the RMS current I_1, while the red curve is the RMS current I_2. When the lower resonant splitting frequency f_L is used as the excitation frequency, the magnitude of RMS current I_1 is greater than that of RMS current I_2. However, when the higher resonant splitting frequency f_H is used as the excitation frequency, the magnitude of RMS current I_1 is always smaller than that of RMS current I_2. The possible reason is that the variation rate of capacitive and inductive impedance is different with the frequency variation.

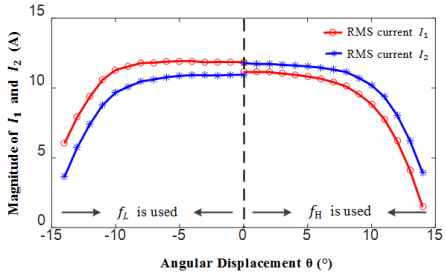

Fig. 19. Simulation result from PSIM: the magnitudes of I_1 and I_2 corresponding to different angular displacement θ .

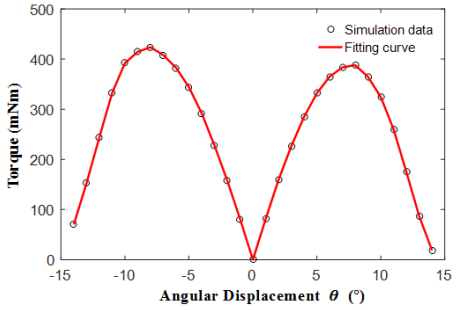

Fig. 20. Simulation result from ANSYS Maxwell: the magnitude of average torque corresponding to different angular displacement θ in a pole pair.

The magnitude of the average torque is determined by not only the attenuation coefficient γ and the magnitudes of RMS current I_1 and I_2, but the relative position between the stator resonant circuit and the rotor resonant circuit. As is shown in Fig. 20, the magnitude of the average torque corresponding to different angular displacement θ is further simulated in ANSYS Maxwell based on the data obtained in Fig. 17 and 19. Fig. 20 shows that when the stator and rotor resonant circuits are aligned, i.e. the angular displacement θ is 0°, no torque would be developed. Besides, the maximum attraction force is developed at the angular displacement θ of $-8°$, and the maximum repulsion force is developed at angular displacement θ of 8°. For one pole pair in the proposed MRCM, the maximum value of average torque is around 400 mNm with the input power of about 60 watts.

The magnitude of the simulated torque ripple in a pole pair is relatively large. Nevertheless, the overall torque ripple could be much smaller with the careful manipulation of pole arrangement and control strategy in a multi-pole MRCM.

C. Transient Process and Steady State

To investigate the transient process of the proposed MRCM, a specific example with the angular displacement θ $\pm 5°$ is presented here. Using the parameters listed in Table I, simulation results are obtained from PSIM. As is shown in Fig. 21, using the lower resonant splitting frequency f_L or higher resonant splitting frequency f_H, the currents $i_1(t)$ and $i_2(t)$ of stator and rotor resonant circuits can reach a steady state with the amplitude of around 16 A. Moreover, since the total number of period to reach the steady state is constant, to use the higher resonant splitting frequency f_H could reach the full resonance in a shorter time than to use lower resonant splitting frequency f_L. As tens of period are necessary to reach the full resonance, for different rotational speed, it is essential to select a natural frequency f_0 which can guarantee that the stator and rotor resonant circuit have sufficient time to fulfill the full resonance. In other words, a higher rotational speed demands a higher designed natural frequency f_0 to maintain the full resonance.

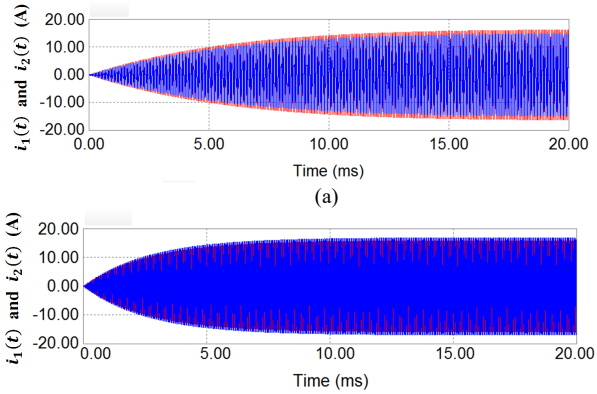

Fig. 21. Simulation result from PSIM: transient process of the currents of red curve $i_1(t)$ and blue curve $i_2(t)$ during the period from 0 ms to 20 ms in PSIM. (b) a lower resonant splitting frequency f_L is used when the angular displacement θ is $-5°$. (b) a higher resonant splitting frequency f_H is used when the angular displacement θ is 5°.

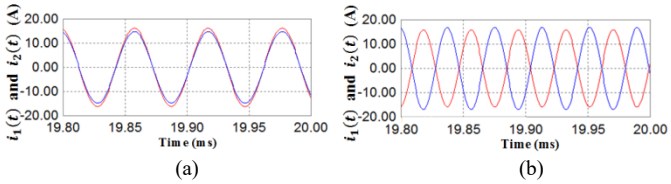

Fig. 22. Simulation result from PSIM: steady state of the currents of red curve $i_1(t)$ and blue curve $i_2(t)$ during the period from 19.8 ms to 20 ms. (a) a lower resonant splitting frequency f_L is used when the angular displacement θ is $-5°$. (b) a higher resonant splitting frequency f_H is used when the angular displacement θ is 5°.

Fig. 22 presents a zoom-in view of Fig. 21 during the period from 19.8 ms to 20 ms. It is clear to identify that using lower resonant splitting frequency f_L provides an approximately 0° phase difference δ between $i_1(t)$ and $i_2(t)$, while using higher

resonant splitting frequency f_L provides an approximately 180° phase difference δ between $i_1(t)$ and $i_2(t)$.

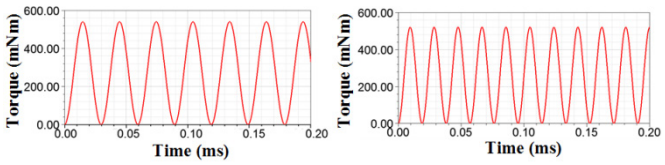

(a) (b)

Fig. 23. Simulation result from ANSYS Maxwell: steady state of torque corresponding to Fig. 22. (a) a lower resonant splitting frequency f_L is used when the angular displacement θ is $-5°$. (b) a higher resonant splitting frequency f_H is used when the angular displacement θ is 5°

Based on the magnitude of currents $i_1(t)$ and $i_2(t)$, a transient simulations in ANSYS Maxwell are conducted to perform the torque estimation. Fig. 23(a) demonstrates the simulated torque when a lower resonant splitting frequency f_L is used at the angular displacement θ of $-5°$. The average torque is calculated to be 344 mNm. Besides, when a higher resonant splitting frequency f_H is used at the angular displacement θ of 5°, the average torque is calculated to be 331 mNm as shown in Fig. 23(b). These average torque values are the same as the data shown in Fig. 20. Above transient and steady state simulations have further verified the feasibility of the proposed MRCM.

D. Simulation Results of a Complete MRCM

Based on design parameters detailed in Table I, a MRCM simulation model, consisting of 10 stator poles and 8 rotor poles, is developed in ANSYS Maxwell. As shown in Fig. 24, the 10 stator poles are divided into 5 phases (A, B, C, D and E) while the 8 rotor poles are divided into 4 phases (W, X, Y, Z). With the proposed pole arrangement, the excitation sequence is well manipulated such that each stator phase would have a working range of 9° rotation angle with the corresponding angular displacement θ being $-12^\circ \sim -3^\circ$ for attraction force and $3^\circ \sim 12^\circ$ for repulsion force. The sequence of the effective stator phase is a repetition of the order B-A-E-D-C, and the sequence of the effective rotor phase is a repetition of the order X-W-Z-Y. However, the effective stator and rotor phases would have different combinations depending on the rotor position.

TABLE I
DESIGN PARAMETERS OF PROPOSED MRCM

Symbol	Parameters	Values
	2D Model Specifications	
-	model depth	200 mm
-	outer radius of stator	150 mm
-	outer radius of rotor	130 mm
-	air gap	1 mm
-	section area of copper winding	400 mm^2
-	number of stator poles	10
-	number of rotor poles	8
-	estimated weight	37.8 kg
	Resonant Circuit in a Pole Pair	
N_1, N_2	number of turns of stator and rotor winding	100, 100
L_1, L_2	inductance of stator and rotor winding	1.1093 mH, 1.1467 mH
C_1, C_2	capacitance in stator and rotor resonant circuit	0.0571 μF, 0.0552 μF
R_1, R_2	internal resistance of stator and rotor winding	0.2 Ω, 0.2 Ω
f_0	natural frequency	20 kHz
	Excitation	
V	RMS value of voltage source	6 V
-	f_L at $-5°$ angular displacement θ	16.786 kHz
-	f_H at 5° angular displacement θ	26.251 kHz

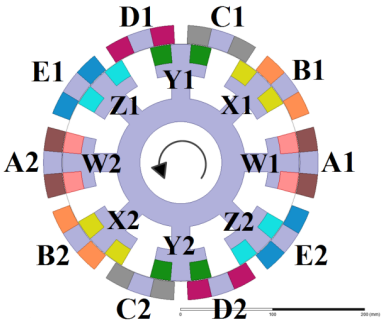

Fig. 24. Simulation model of the proposed MRCM in ANSYS Maxwell when the rotation angle is 0°.

TABLE II
EXCITATION SEQUENCE

Repulsion Force Using Higher Resonant Splitting Frequency f_H:							
Rotation Angle	0°–3°	3°–12°	12°–21°	21°–30°	30°–39°	39°–48°	48°–57°
Effective Stator Phase	B	A	E	D	C	B	A
Effective Rotor Phase	X	W	Z	Y	X	W	Z
Attraction Force Using Lower Resonant Splitting Frequency f_L:							
Rotation Angle Phase	0°–6°	6°–15°	15°–24°	24°–33°	33°–42°	42°–51°	51°–57°
Effective Stator Phase	E	D	C	B	A	E	D
Effective Rotor	Z	Y	X	W	Z	Y	X

Besides, as shown in Table II, at each time instant only two nonadjacent stator phases are powered to generate rotational force, where one stator phase produces repulsion force using higher resonant splitting frequency f_H, the other stator phase produces attraction force using lower resonant splitting frequency f_L. Specifically, when the rotation angle is 0° as demonstrated in Fig. A, the angular displacement θ between stator phase B and rotor phase X is 9°, and a specific higher resonant splitting frequency f_H is used to power stator phase B to generate repulsion force. The angular displacement θ between stator phase E and rotor phase Z is 9°, and a specific lower resonant splitting frequency f_L is used to power stator phase E to generate attraction force.

Considering the large torque ripple in one pole pair as shown in Fig. 23, the excitation for two poles (B1 and B2) of stator phase B would have a phase different of $\frac{\pi}{2}$ to reduce the torque ripple: $V\sin(2\pi f_H t)$ and $V\sin(2\pi f_H t + \frac{\pi}{2})$. Similarly, the excitation for two poles (E1 and E2) of stator phase E would also have a phase different of $\frac{\pi}{2}$ to reduce the torque ripple: $V\sin(2\pi f_L t)$ and $V\sin(2\pi f_L t + \frac{\pi}{2})$.

When the rotor speed is 1,000 rpm, the simulation result of output torque is obtained as shown in Fig. 25. Compared to the simulated torque in one pole pair as shown in Fig. 20, the torque ripple in Fig. 25 is reduced significantly. The torque ripple could be further reduced by using more number of poles and more sophisticated control strategy. More simulation results are presented in Table III.

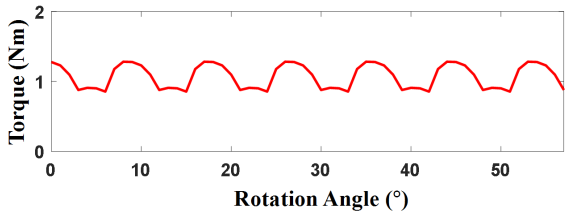

Fig. 25. Simulation results of proposed MRCM from ANSYS Maxwell: output torque for different rotation angle.

TABLE III
SIMULATION RESULTS

Parameters	Values
rotor speed	1000 rpm
input power	305.44 W
power factor	1
average output torque	1.0678 Nm
torque ripple	39.32%
efficiency	36.61%
output power density	2.96 W/kg

E. Comparison with Conventional Induction Motor

While to the best of authors' knowledge there is no existing coreless and magnetless motor available for comparison, it would be difficult and unfair to make a thorough comparison between a coreless and magnetless electric motor and a conventional induction motor with cores in high permeability. Instead, a simple comparison with a conventional induction motor using ANSYS Maxwell simulation is provided here to further illustrate the relative merits of the proposed MRCM.

The drive system of the proposed MRCM is similar to the one for conventional electric motors consisting of an AC/DC rectifier, a DC bus, a DC/AC inverter and a controller with the main differences of requiring (1) a higher switching frequency to enable the efficient wireless power transfer between stator resonant circuits and rotor resonant circuits, and (2) a high revolution encoder and a fast digital controller to track the rotor-position-dependent excitation frequency. Therefore, for the same power level, their weight would be comparable while the power losses in the drive of the conventional induction motor would be smaller due to its lower switching frequency.

A 2D simulation model of a conventional induction motor as shown in Fig. 26 was developed with specifications comparable to the proposed MRCM. Table IV lists the design parameters of this conventional induction motor including 2D model specifications and rated parameters.

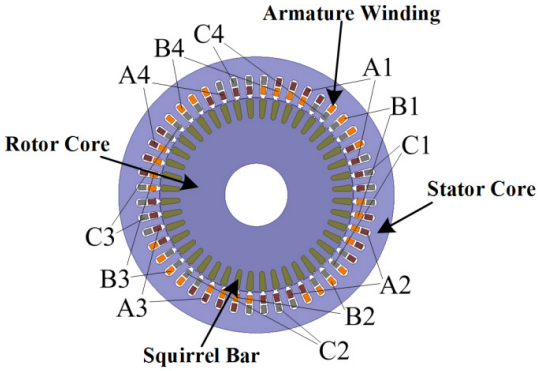

Fig. 26. Simulation model of the conventional induction motor in ANSYS Maxwell.

For comparison purpose, the operating conditions of the conventional induction motor were adjusted to be comparable to the proposed MRCM with same input power of 305 W and rotor speed of 1000 rpm. The efficiency, power factor and output power density of conventional induction motor were then obtained. Besides, with the same output torque, the torque ripple percentage is calculated by using the simulation result as is shown in Fig. 27. Table V summaries the quantitive comparison between the proposed MRCM and the conventional induction motor.

TABLE IV
DESIGN PARAMETERS OF CONVENTIONAL INDUCTION MOTOR

Parameters	Values
2D Model Specifications	
model depth	200 mm
outer radius of stator	150 mm
outer radius of rotor	111.5 mm
length of air gap	1 mm
number of stator slots	48
number of rotor bars	44
number of phases	3
number of stator pole pairs	2
turns of stator conductors	15
core material	MG19_24
phase resistance	0.67 Ω
phase inductance	0.23 mH
estimated weight	73.8 kg
Rated Parameters	
input power	8.41 kW
input voltage	310.27 V
excitation frequency	50 Hz
rotation speed	1453.66 rpm
torque	49.22 Nm
efficiency	89.1%
power factor	0.93
output power density	101.53 W/kg

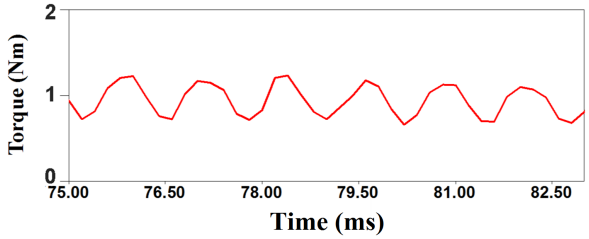

Fig. 27. Simulation results of conventional induction motor from ANSYS Maxwell: output torque at steady state.

TABLE V
COMPARISON BETWEEN PROPOSED MRCM AND CONVENTIONAL INDUCTION MOTOR

Parameters	Proposed MRCM	Conventional Induction Motor
efficiency	36.61 %	73.52 %
power factor	1	0.896
output power density	2.96 W/kg	3.04 W/kg
torque ripple	39.32 %	60.41 %

From Table V, it can be concluded that one of the promising characteristics of proposed MRCM is the inherent unity power factor. With a similar output torque, the torque ripple percentage of the proposed MRCM is smaller than the convention induction motor. Besides, the output power density of the proposed MRCM is almost the same as the conventional induction motor. However, the efficiency of the proposed

MRCM is significantly lower than the conventional induction motor, mainly due to the compromise for the proposed coreless design. Nevertheless, this can be improved by making full use of rotor space, reducing the conductor resistance, and especially employing suitable cores with high permeability.

V. Conclusion

This paper presents a novel magnetic resonant coupling motor (MRCM) constructed without any ferrous or permanent-magnet core. As an elementary and essential part of the proposed MRCM, a pole pair is analyzed elaborately in terms of the selection of resonant topology, the force magnitude and direction, and the frequency splitting phenomenon; besides, the underlying operation principle has been developed from the perspective of a pole pair. Following the proposed design procedures, the feasibility of the proposed MRCM is fully validated using computer simulations in MATLAB, PSIM and ANSYS Maxwell. A rough comparison with the conventional induction motor was provided to further illustrate the relative merits of the proposed MRCM. Simulation results obtained so far are stimulating and the proposed MRCM could well be a promising start for a new generation of future electric motor. On-going research is now focused on the optimization of the motor structure and pole ratio as well as the realization of sophisticated position tracking and frequency control. Furthermore, it is possible to enhance the proposed MRCM by employing suitable cores material with high permeability.

References

[1] Z. Q. Zhu and D. Howe, "Electrical machines and drives for electric, hybrid, and fuel cell vehicles," *Proc. IEEE,* vol. 95, no. 4, pp. 746-765, Apr. 2007.

[2] J. Liu, K. W. Chan, C. Y. Chung, N. H. L. Chan, M. Liu, and W. Xu, "Single-stage wireless-power-transfer resonant converter with boost bridgeless power-factor-correction rectifier," *IEEE Trans. Ind. Electron.,* vol. 65, no. 3, pp. 2145-2155, Mar. 2018.

[3] Y. Li, R. Mai, L. Lu, T. Lin, Y. Liu, and Z. He, "Analysis and transmitter currents decomposition based control for multiple overlapped transmitters based WPT systems considering cross couplings," *IEEE Trans. Power Electron.,* vol. 33, no. 2, pp. 1829-1842, Feb. 2018.

[4] Y. Li, R. Mai, L. Lu, and Z. He, "Active and reactive currents decomposition-based control of angle and magnitude of current for a parallel multiinverter IPT system," *IEEE Trans. Power Electron.,* vol. 32, no. 2, pp. 1602-1614, Feb. 2017.

[5] N. Tesla, "Apparatus for transmitting electrical energy," ed. U.S. Patent 1119732 A, May 1907.

[6] A. Kurs, A. Karalis, R. Moffatt, J. D. Joannopoulos, P. Fisher, and M. Soljačić, "Wireless power transfer via strongly coupled magnetic resonances," *Sci. Express,* vol. 317, no. 5834, pp. 83-86, Jun. 2007.

[7] J. Y. Lee and B. M. Han, "A bidirectional wireless power transfer EV charger using self-Resonant PWM," *IEEE Trans. Power Electron.,* vol. 30, no. 4, pp. 1784-1787, Apr. 2015.

[8] D. H. Tran, V. B. Vu, and W. Choi, "Design of a high-efficiency wireless power transfer system with intermediate coils for the on-board chargers of electric vehicles," *IEEE Trans. Power Electron.,* vol. 33, no. 1, pp. 175-187, Jan. 2018.

[9] K. Agarwal, R. Jegadeesan, Y. X. Guo, and N. V. Thakor, "Wireless power transfer strategies for implantable bioelectronics," *IEEE Rev. Biomed. Eng.,* vol. 10, pp. 136-161, Mar. 2017.

[10] D. Ahn and S. Hong, "Wireless power transmission with self-regulated output voltage for biomedical implant," *IEEE Trans. Ind. Electron.,* vol. 61, no. 5, pp. 2225-2235, May 2014.

[11] Y. Zhang and Z. Zhao, "Frequency splitting analysis of two-coil resonant wireless power transfer," *IEEE Antennas Wireless Propag. Lett.,* vol. 13, pp. 400-402, Mar. 2014.

[12] H. Runhong, Z. Bo, Q. Dongyuan, and Z. Yuqiu, "Frequency splitting phenomena of magnetic resonant coupling wireless power transfer," *IEEE Trans. Magn.,* vol. 50, no. 11, pp. 1-4, Nov. 2014.

[13] D. Ahn and S. Hong, "A study on magnetic field repeater in wireless power transfer," *IEEE Trans. Ind. Electron.,* vol. 60, no. 1, pp. 360-371, Jan. 2013.

[14] A. P. Sample, D. A. Meyer, and J. R. Smith, "Analysis, experimental results, and range adaptation of magnetically coupled resonators for wireless power transfer," *IEEE Trans. Ind. Electron.,* vol. 58, no. 2, pp. 544-554, Feb. 2011.

[15] Y. Zhang, Z. Zhao, and K. Chen, "Frequency-splitting analysis of four-coil resonant wireless power transfer," *IEEE Trans. Ind. Appl.,* vol. 50, no. 4, pp. 2436-2445, Aug. 2014.

[16] W. Q. Niu, J. X. Chu, W. Gu, and A. D. Shen, "Exact analysis of frequency splitting phenomena of contactless power transfer systems," *IEEE Trans. Circuits Syst. I, Reg. Papers,* vol. 60, no. 6, pp. 1670-1677, Jun. 2013.

[17] L. Hongchang, L. Jie, W. Kangping, C. Wenjie, and Y. Xu, "A maximum efficiency point tracking control scheme for wireless power transfer systems using magnetic resonant coupling," *IEEE Trans. Power Electron.,* vol. 30, no. 7, pp. 3998-4008, Jul. 2015.

[18] S. Huang, Z. Li, and K. Lu, "Frequency splitting suppression method for four-coil wireless power transfer system," *IET Power Electron.,* vol. 9, no. 15, pp. 2859-2864, Dec. 2016.

[19] Y. L. Lyu, F. Y. Meng, G. H. Yang, B. J. Che, Q. Wu, L. Sun*, et al.*, "A method of using nonidentical resonant coils for frequency splitting elimination in wireless power transfer," *IEEE Trans. Power Electron.,* vol. 30, no. 11, pp. 6097-6107, Nov. 2015.

[20] A. Abdolkhani, A. P. Hu, and N. K. C. Nair, "A double stator through-hole type contactless slipring for rotary wireless power transfer applications," *IEEE Trans. Energy Convers.,* vol. 29, no. 2, pp. 426-434, Jun. 2014.

[21] H. Nguyen, J. I. Agbinya, and J. Devlin, "FPGA-based implementation of multiple modes in near field inductive communication using frequency splitting and MIMO configuration," *IEEE Trans. Circuits Syst. I, Reg. Papers,* vol. 62, no. 1, pp. 302-310, Jan. 2015.

[22] M. Sato, G. Yamamoto, D. Gunji, T. Imura, and H. Fujimoto, "Development of wireless in-wheel motor using magnetic resonance coupling," *IEEE Trans. Power Electron.,* vol. 31, no. 7, pp. 5270-5278, Jul. 2016.

[23] T. Diekhans and R. W. D. Doncker, "A dual-side controlled inductive power transfer system optimized for large coupling factor variations and partial load," *IEEE Trans. Power Electron.,* vol. 30, no. 11, pp. 6320-6328, Nov. 2015.

[24] Y. C. Hsieh, Z. R. Lin, M. C. Chen, H. C. Hsieh, Y. C. Liu, and H. J. Chiu, "High-efficiency wireless power transfer system for electric vehicle applications," *IEEE Trans. Circuits Syst. II, Exp. Briefs,* vol. 64, no. 8, pp. 942-946, Aug. 2017.

[25] R. Jegadeesan and Y. X. Guo, "Topology selection and efficiency improvement of inductive power links," *IEEE Trans. Antennas Propag.,* vol. 60, no. 10, pp. 4846-4854, Oct. 2012.

Ming Liu received his B.Eng. degree in electrical engineering from Qingdao University, Qingdao, China, in 2014. He is currently pursuing the Ph.D. degree in electrical engineering at The Hong Kong Polytechnic University, Hong Kong.

His research interests include electric machine design, model predictive control for power converters and motor drives, and wireless power transfer.

Ka Wing Chan (M'98) received the B.Sc. (Hons) and Ph.D. degrees in electronic and electrical engineering from the University of Bath, U.K., in 1988 and 1992, respectively. He currently is an Associate Professor and Associate Head in the Department of Electrical Engineering of the Hong Kong Polytechnic University. His general research interests include power system stability, analysis and control, power grid integration, security, resilience and optimization, demand response management, etc.

Jiefeng Hu (S'12 – M'14 – SM'16) received the Ph.D. degree in electrical engineering from University of Technology Sydney (UTS), Australia, in 2013. From 2011 to 2013, he was involved in the research of minigrids in Commonwealth Scientific and Industrial Research Organization (CSIRO), Newcastle, Australia. Currently he is an Assistant Professor at Hong Kong Polytechnic University, Hong Kong. He served as committee member and session chair in several international conferences. He also serves as reviewer for various IEEE Transactions.

His research interests include power electronics, renewable energy, and smart microgrids.

Qifang Lin received her B.S. degree from the Department of information and control, Xi'an University of Architecture and Technology, Xi'an, China, in 2014, and the Master's degree from Department of electrical engineering, The Hong Kong Polytechnic University, Hong Kong, in 2015. She is currently pursuing the Ph.D. degree in electrical engineering at The Hong Kong Polytechnic University, Hong Kong.

Her research interests include electrical machine design and their performances optimization especially synchronous permanent magnet machine.

Junwei Liu received his B.Eng. degree in water conservancy and hydropower engineering from Huazhong University of Science and Technology, China, in 2012, and the Ph.D. degree in Electrical Engineering from The Hong Kong Polytechnic University, Hong Kong, in 2018. Currently, he works as a postdoctoral fellow in The Hong Kong Polytechnic University.

His research interests include wireless power transfer, AC-DC single-stage topologies, and high power DC-DC conversions.

Wenzheng Xu (S'16) received his B.E.E. degree from the Department of Electrical Engineering , Beijing Jiaotong University, Beijing, China, in 2012, and the M.Sc. degree from Department of Electrical and Electronic Engineering, The University of Hong Kong, Hong Kong, in 2013. From September 2013 to June 2015, he was a research associate in the Hong Kong Polytechnic University working for a series of high-power converters and EV fast charging projects. He is currently pursuing the Ph.D. degree in electrical engineering at The Hong Kong Polytechnic University, Hong Kong.

His research interest includes power electronics topologies, dual-active-bridge converters, bi-directional Z-source converters, control for switch mode converters and its application in microgrid.